Thermodynamics, structure, dynamics, and freezing of Mg_2SiO_4 liquid at high pressure

Nico P. de Koker [a,*], Lars Stixrude [a,1], Bijaya B. Karki [b,c]

[a] *Department of Geological Sciences, University of Michigan, Ann Arbor, MI 48109, USA*
[b] *Department of Computer Science, Louisiana State University, Baton Rouge, LA 70803, USA*
[c] *Department of Geology and Geophysics, Louisiana State University, Baton Rouge, LA 70803, USA*

Abstract

We perform first principles molecular dynamics simulations of Mg_2SiO_4 liquid and crystalline forsterite. On compression by a factor of two, we find that the Grüneisen parameter of the liquid increases linearly from 0.6 to 1.2. Comparison of liquid and forsterite equations of state reveals a temperature-dependent density crossover at pressures of ∼12–17 GPa. Along the melting curve, which we calculate by integration of the Clapeyron equation, the density crossover occurs within the forsterite stability field at $P = 13$ GPa and $T = 2550$ K. The melting curve obtained from the root mean-square atomic displacement in forsterite using the Lindemann law fails to match experimental or calculated melting curves. We attribute this failure to the liquid structure that differs significantly from that of forsterite, and which changes markedly upon compression, with increases in the degree of polymerization and coordination. The mean Si coordination increases from 4 in the uncompressed system to 6 upon twofold compression. The self-diffusion coefficients increase with temperature and decrease monotonically with pressure, and are well described by the Arrhenian relation. We compare our equation of state to the available highpressure shock wave data for forsterite and wadsleyite. Our theoretical liquid Hugoniot is consistent with partial melting along the forsterite Hugoniot at pressures 150–170 GPa, and complete melting at 170 GPa. The wadsleyite Hugoniot is likely sub-liquidus at the highest experimental pressure to date (200 GPa).
© 2008 Elsevier Ltd. All rights reserved.

1. INTRODUCTION

The Earth's mantle is almost entirely solid, yet liquids play a disproportionately large role in our understanding of terrestrial chemical and thermal evolution. Silicates melt incongruently, and in the shallow mantle, the partial melt is readily separated from the residuum as a result of the large density contrast and low viscosity of the liquid. To accurately describe these processes, knowledge of the changes in liquid physical properties with pressure and temperature is needed, especially the density, Grüneisen parameter, chemical diffusivity and melting temperature. Furthermore, an understanding of liquid structure that ultimately governs these physical properties is key to predicting properties at conditions previously unexplored, and also offers deep insight into the physics of the liquid state.

Olivine and its polymorphs of dominantly Mg_2SiO_4 composition make up approximately 60% of the upper mantle and transition zone. With increasing pressure, the eutectic composition on the MgO–SiO$_2$ join moves toward Mg_2SiO_4 (Ohtani and Kumazawa, 1981; Kato and Kumazawa, 1985; Presnall and Gasparik, 1990). The properties of Mg_2SiO_4 liquid are thus crucial to deep earth studies involving a liquid phase. These include magma ocean dynamics, lunar formation, and mantle melting as the source for komatiitic and basaltic magmas. Buoyantly stable partial melt has been proposed to exist atop the 410 km discontinuity on the basis of seismic observations

---

* Corresponding author. Fax: +1 734 763 4690.
  E-mail address: dekoker@umich.edu (N.P. de Koker).
[1] Now at Department of Earth Sciences, University College London, London WC1E 6BT, UK.

(Revenaugh and Sipkin, 1994; Song et al., 2004). In addition, the discovery of an ultra-low-velocity zone (ULVZ) at the core–mantle boundary (CMB) (Garnero and Helmberger, 1995; Williams and Garnero, 1996) has lead to the speculation of the presence of partial melt in the bottom most part of the mantle. Indeed, estimates of the mantle geotherm in the lowermost mantle are similar to estimates of the lower mantle solidus (Holland and Ahrens, 1997; Luo et al., 2004; Stixrude and Karki, 2005).

The high melting temperature of forsterite (2163 ± 25 K; Bowen and Andersen, 1914) has made accurate *in situ* experimental measurement of Mg_2SiO_4 liquid properties difficult. The volume at ambient pressure and its pressure and temperature derivatives are estimated from experimental measurements at lower temperature and more silica-rich compositions, combined with the assumption of linear additivity of partial molar properties (Lange and Carmichael, 1987; Lange, 1997; Ai and Lange, in press), or from fusion curve analysis and calorimetric data (Bottinga, 1985). The value of C_P measured for the supercooled liquid (225 J mol^{-1} K^{-1}; Tangeman et al., 2001) differs significantly from the model value calculated from partial molar heat capacities (285–295 J mol^{-1} K^{-1}; Stebbins et al., 1984; Lange and Navrotsky, 1992). Studies of non-crystalline structure have been limited to Mg_2SiO_4 glass (Cooney and Sharma, 1990; Kohara et al., 2004).

Here we apply first principles molecular dynamics to simulate Mg_2SiO_4 liquid and forsterite at pressures and temperatures relevant to the mantle. We investigate the equation of state, liquid structure, and transport properties and compare with experiments and previous results based on semi-empirical inter atomic force models. By combining the liquid equation of state with that of forsterite, calculated using the same method, we integrate the Clapeyron equation to obtain the forsterite melting curve.

2. COMPUTATIONAL TECHNIQUE

The power and robustness of density functional theory (DFT) as a tool for determining the properties of earth materials at conditions relevant to planetary interiors have been extensively explored (Stixrude, 2001; Gillan et al., 2006). DFT was recently applied in combination with Born–Oppenheimer molecular dynamics to the simulation of silicate liquids over the entire mantle pressure–temperature regime (Stixrude and Karki, 2005; Karki et al., 2007).

DFT is based on the Hohenberg–Kohn theorem (Hohenberg and Kohn, 1964; Kohn and Sham, 1965), through which the wave function and total energy may be expressed as a unique functional of the ground state electron density. Although the theorem is exact, approximations are needed to account for the unknown exchange-correlation functional. In this study we adopt the most widely tested approximation, the local density approximation (LDA, Ceperley and Alder, 1980).

The influence of the core electronic wave functions of Mg, Si and O is approximated using ultrasoft pseudopotentials with core radii of 1.06, 0.95 and 0.82 Å, and valence shells representing the $3s^2$, $3s^23p^2$ and $2s^22p^4$ electrons, respectively (Kresse and Hafner, 1994), as implemented in

the VASP code (Kresse and Furthmüller, 1996). We perform molecular dynamics in the canonical ensemble (constant *NVT*), via a thermostat (Nosé, 1984). In order to make simulation with systems of sufficient size computationally feasible, the size of the plane-wave basis set is limited to a cutoff energy $E_{cut} = 400$ eV, for which we account by applying a finite basis set (Pulay) correction (Gomes Dacosta et al., 1986; Francis and Payne, 1990) to the calculated pressures (see below).

Simulations contain 112 atoms (16 formula units) with periodic boundary conditions (Fig. 1). The initial condition is a $2 \times 1 \times 2$ supercell of forsterite homogeneously strained to a cubic cell shape and the desired volume. The Brillouin zone is sampled at the gamma point only. We simulate the liquid at volumes of $V/V_X = 1.2, 1.1, 1.0, 0.9, 0.8, 0.7, 0.6$ and 0.5 where $V_X = 52.36$ cm^3/mol is an estimate of the volume of Mg_2SiO_4 liquid at the ambient melting point (Lange and Carmichael, 1987). The initial configuration is melted at 6000 K, and then cooled isochorically to 3000 and 4000 K. We also perform simulations of crystalline forsterite at 1000, 2000 and 3000 K, and at volumes $V/V_X = 1.0, 0.9, 0.8$ and 0.7. We initiate crystalline simulations with the cell shape obtained by static structural relaxation at each volume, and then adjust cell parameters until the stress tensor is hydrostatic to within statistical uncertainty (Oganov et al., 2001). The phase present in the simulation (crystal or liquid) is verified by inspection of the radial distribution function and the mean-square displacement. Simulations of both liquid and solid are performed using a time step $\Delta t = 1$ fs, with each simulation running for at least 3000 time steps. The first 600 steps allow the system to converge, with equilibrium properties calculated over the remaining time. We estimate the uncertainty in the energy (E) and pressure (P) by applying the blocking method (Flyvberg and Petersen, 1989). Tests of convergence with respect to system size (70 and 336 atom supercells), run duration (6 ps), initial configuration (strained ringwoodite) and k-point sampling ($2 \times 2 \times 2$ Monkhorst and Pack (1976) grid) show that variations are well within the mean statistical uncertainty of the simulations ($\sigma_E = 8.8$ kJ/mol; $\sigma_P = 1.5$ GPa). Slow cooling over 3000 fs from 6000 to 3000 K showed no cooling rate dependence of the thermodynamic or structural properties.

Two corrections are applied to the pressures calculated in the simulations as follows:

$$P(V) = P_{MD}(V) + P_{Pulay}(V) + P_{emp}(V). \qquad (1)$$

We compute the Pulay correction as

$$P_{Pulay}(V) = P_S(V; E_{cut} = 600 \text{ eV}) - P_S(V; E_{cut} = 400 \text{ eV}), \qquad (2)$$

where P_S is the static pressure of the fully relaxed structure of forsterite computed with a $2 \times 2 \times 2$ Monkhorst Pack k-point mesh, and 600 eV as has been found in previous studies to yield fully converged results (Karki et al., 2001). We find that P_{Pulay} increases monotonically from 2.6 GPa at $V/V_X = 1.0$–5.1 GPa at $V/V_X = 0.5$. Values calculated for different atomic configurations obtained from the simulations, as well as for wadsleyite and ringwoodite, differ from the forsterite value by less than 0.2 GPa. The
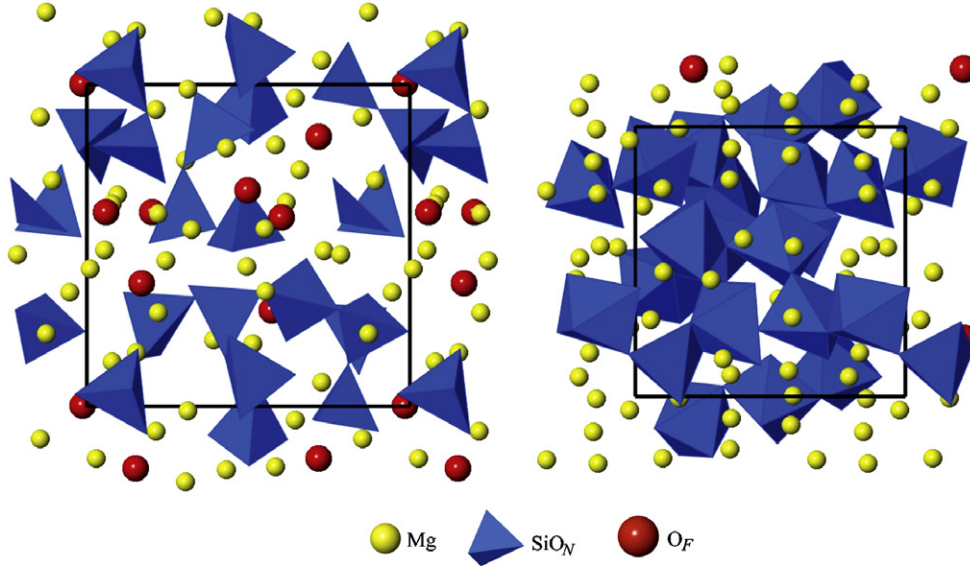
Fig. 1. Snapshots of the simulated liquid at 3000 K, for volumes $V/V_X = 1.0$ and $V/V_X = 0.5$. The uncompressed structure is very open, with Si almost entirely fourfold coordinated. Tetrahedra are mostly free-floating, with dimers and a four-membered chain also visible. The compressed structure is more densely packed, with Si mostly sixfold coordinated. Polyhedra are highly polymerized, some sharing edges. Free oxygen atoms (red spheres) are less abundant at higher pressures. (For interpretation of the references to color in this figure legend, the reader is referred to the web version of this paper.)

empirical correction accounts for the well known and systematic over-binding of LDA (Karki et al., 2001; Oganov et al., 2001) and is computed as

$$P_{\text{emp}} = -P_S(V_{\text{exp}}; E_{\text{cut}} = 600 \text{ eV}), \tag{3}$$

where V_{exp} is the experimental zero-pressure volume of forsterite at static conditions computed via the thermodynamic model of Stixrude and Lithgow-Bertelloni (2005). For forsterite we find $P_{\text{emp}} = 1.6$ GPa. Values calculated for wadsleyite and ringwoodite are 1.4 and 1.7 GPa, respectively.

We fit the simulation pressure and internal energy results to the Mie-Grüneisen equation of state,

$$P(V, T) = P_C(V, T_0) + \frac{\gamma(V)C_V(V)}{V}[T - T_0], \tag{4}$$

$$E(V, T) = E_0 + E_C(V, T_0) + C_V(V)[T - T_0], \tag{5}$$

$$P_C(V, T_0) = 3K_0 f(1 + 2f)^{5/2}[1 + a_1 f + \cdots], \tag{6}$$

$$E_C(V, T_0) = T_0 \int_{V_0}^{V} \frac{\gamma(V')C_V(V')}{V'} \, dV'$$
$$+ 9K_0 V_0 f^2 \left[\frac{1}{2} + \frac{a_1}{3} f + \cdots \right], \tag{7}$$

$$a_1 = \frac{3}{2}[K'_0 - 4], \tag{8}$$

$$f = \frac{1}{2}\left[\left(\frac{V_0}{V} \right)^{2/3} - 1 \right], \tag{9}$$

where the expression for the internal energy follows from the Eulerian finite strain expansion of the Helmholz free energy, F, (Birch, 1952; Stixrude and Bukowinski, 1990), the Euler relation, $E = F + TS$, and the Maxwell identity $(\partial S/\partial V)_T = (\partial P/\partial T)_V$. E_0, V_0, K_0, and K'_0 are, respectively, the internal energy, volume, isothermal bulk modulus (K_T), and its first pressure derivative at zero pressure and temperature T_0. The isochoric heat capacity (C_V) and Grüneisen parameter (γ), are determined from our simulations as the dependence of internal energy and pressure on temperature at constant volume, and are found to be linear to within our resolution:

$$C_V = \left(\frac{\partial E}{\partial T} \right)_V, \tag{10}$$

$$\frac{\gamma}{V} = \left(\frac{\partial P}{\partial E} \right)_V. \tag{11}$$

The volume dependence of C_V and γ are described accurately as

$$C_V(V) = C_V(V_X) + C'_V \left[\frac{V}{V_X} - 1 \right] + \cdots, \tag{12}$$

$$\gamma(V) = \gamma(V_X) + \gamma' \left[\frac{V}{V_X} - 1 \right] + \cdots. \tag{13}$$

We estimate the uncertainty in a thermodynamic quantity at a given volume and temperature by repeated fitting of the equation of state to a Monte-Carlo sampling of the simulation data within its error estimates (values converge after about 10^4 iterations).

The melting curve is computed via the Clausius–Clapeyron relation

$$\frac{\partial T_M}{\partial P} = \frac{\Delta V}{\Delta H/T_M}, \tag{14}$$

where the volume and enthalpy differences are taken from our simulations, and the integration constant is set to the experimental melting point at ambient conditions (2163 ± 25 K; Bowen and Andersen, 1914). This hybrid approach, in which we take only the initial melting temperature from experiment, and compute the melting

temperature at all other pressures from our simulations is much more efficient than the fully first principles determination of melting temperatures (Sugino and Car, 1995; Alfe, 2005). Moreover, our approach is justified by the good agreement with experimental melting temperatures found in extremely demanding fully first principles computations of melting, which have not yet been attempted on systems as complex as forsterite. In order to compute the melting curve, we compare the properties of the liquid and the solid at constant pressure. This is accomplished via interpolation, and the error in the volume is estimated from that in the pressure as

$$\sigma_V = \left(\frac{\partial V}{\partial P}\right)_T \sigma_P. \tag{15}$$

Our forsterite simulations allow the determination of the mean-square displacement of all the atoms ($\langle u_{rms} \rangle$) as a function of pressure and temperature. Together with the mean inter-atomic distance (a), the Lindemann law melting curve can be calculated in its original formulation (Lindemann, 1910)

$$f_c = \frac{\langle u_{rms} \rangle}{a}, \tag{16}$$

by determining the value of the constant critical fraction (f_c) at the experimental ambient melting point (Gilvarry, 1956).

We calculate the theoretical Hugoniot pressure (P_H), temperature (T_H) and internal energy (E_H) at a given volume (V_H) by iteratively solving Eqs. (4) and (5) to satisfy the Rankine–Hugoniot relation,

$$(E_H - E_R) = -\frac{1}{2}(P_H + P_R)(V_H - V_R), \tag{17}$$

where E_R and V_R is the internal energy and volume of the unshocked sample at reference pressure P_R and temperature T_R.

The self-diffusion coefficient D_N for the N-particle periodic system is computed via

$$D_N = \lim_{t \to \infty} \frac{\langle [r(t)]^2 \rangle}{6t}, \tag{18}$$

where $\langle [r(t)]^2 \rangle$ is the mean-square displacement. The pressure and temperature dependence of D_N is described by the Arrhenius relation,

$$D_N(P, T) = D_N^0 \exp\left[-\frac{E_a + PV_a}{RT}\right], \tag{19}$$

where E_a and V_a are the activation energy and volume. We account for finite size effects in the periodic system by applying a correction based on the Kirkwood–Riseman theory of polymer diffusion (Yeh and Hummer, 2004; Zhang et al., 2004). The diffusivity for an infinitely large system is calculated as

$$D_\infty = D_N + \frac{k_B T \xi}{6\pi\eta L}, \tag{20}$$

where D_N is the diffusivity from the N-particle simulation, ξ is a constant (≈ 2.837297), L is the size of the box and η is the viscosity of the liquid. The viscosity is estimated by the Eyring relation

$$\eta = \frac{k_B T}{D_\infty \lambda}, \tag{21}$$

where λ was found by Lacks et al. (2007) to have a value of $16\,R_O$ for Mg_2SiO_4 liquid, $R_O = 1.4$ Å being a canonical value for the ionic radius of oxygen.

3. RESULTS

3.1. Equation of state

We find the third order expansion in f (Eqs. (4) and (5)) to be sufficient to represent the equation of state results (Fig. 2), with the isochoric heat capacity (C_V) and Grüneisen parameter (γ) as linear functions of volume (Eqs. (12) and (13); Fig. 3). Values of the parameters in Eqs. (4)–(13) for liquid and forsterite are reported in Table 1. Tables 2 and 3 compare theoretical and experimental values for liquid and solid, respectively.

Our computed values of the physical properties of the liquid at the ambient melting point are consistent with previous experimental data (Stebbins et al., 1984; Bottinga, 1985; Lange and Carmichael, 1987; Rivers and Carmichael, 1987; Rigden et al., 1989; Lange, 1997; Tangeman et al., 2001; Ai and Lange, in press). Agreement with the volume, thermal expansivity and bulk modulus is excellent. The computed value of K_0' is much larger than a previous estimate based on fusion curve analysis, and more similar to values found
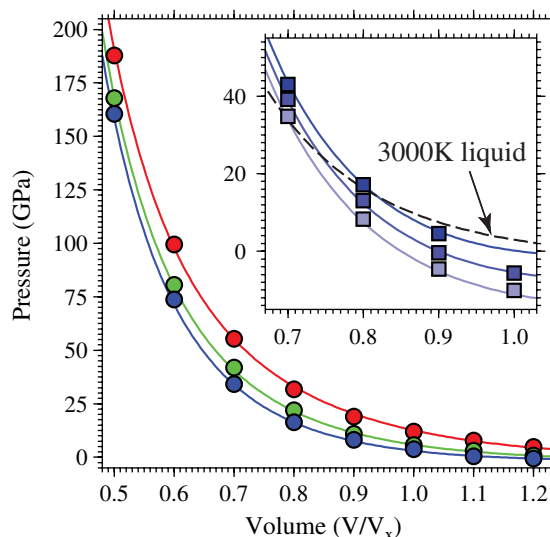

Fig. 2. Equation of state of liquid Mg_2SiO_4. FPMD results are shown by the blue (3000 K), green (4000 K) and red (6000 K) circles, with the Mie-Grüneisen equation fit to these results shown by the colored lines. Note that the $V/V_X = 0.5$; 3000 K point is a glass not included in the fit. A thermal pressure coefficient that increases on compression results in isotherms diverging upon compression. (Inset) FPMD equation of state of forsterite at 1000, 2000 and 3000 K, results shown by squares, Mie-Grüneisen fit by solid blue lines. The broken line is the 3000 K liquid isotherm, which crosses the 3000 K forsterite isotherm close to $V/V_X = 0.8$. The uncertainty in the pressure is similar to the size of the symbols. (For interpretation of the references to color in this figure legend, the reader is referred to the web version of this paper.)
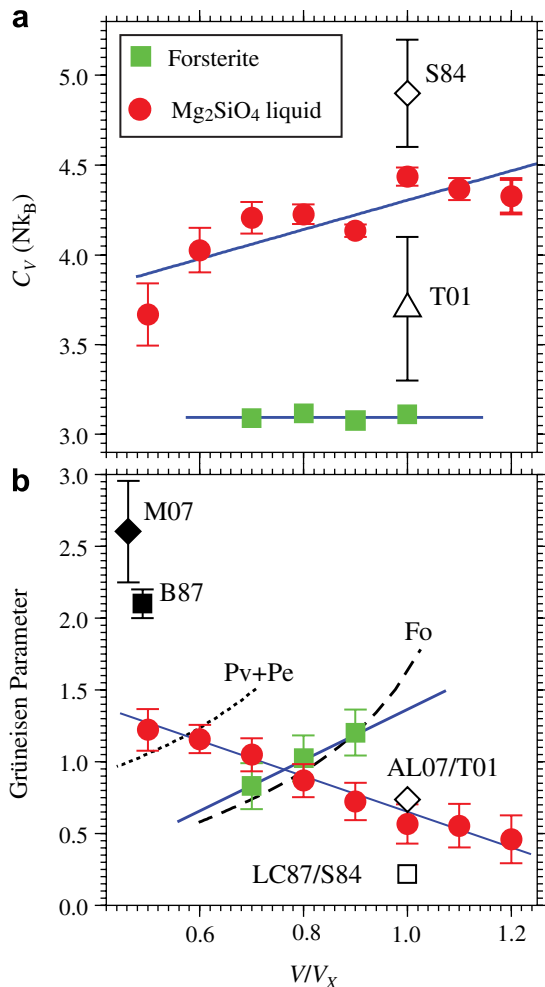
Fig. 3. (a) Isochoric heat capacity (C_V) and (b) Grüneisen paramter (γ) of liquid (red circles) and forsterite (green squares) as a function of volume. Blue curves show the linear fit for the respective properties as given by Eqs. (12) and (13) (see text). At ambient conditions, C_V falls between experimental estimates determined by Stebbins et al. (1984) (S84) and Tangeman et al. (2001) (T01), while γ falls between estimates calculated from the data of Lange (1997), Tangeman et al. (2001), Ai and Lange (in press) (AL07/T01), and Stebbins et al. (1984), Lange (1997), Ai and Lange (in press) (AL07/S84). While liquid γ values increase with compression, high-pressure values are notably less than estimates from shock loading (M07, Mosenfelder et al., 2007; B87, Brown et al., 1987b). Forsterite (Fo) γ values are in excellent agreement with the values calculated from experimental data (dashed line; Stixrude and Lithgow-Bertelloni, 2005), while γ for an isochemical assemblage of perovskite + periclase (Pv + Pe) (dotted line; Stixrude and Lithgow-Bertelloni, 2005) is higher by a value similar to the increasing trend in the liquid. (For interpretation of the references to color in this figure legend, the reader is referred to the web version of this paper.)

for other silicate liquids by direct measurement of the equation of state (Rigden et al., 1989). Our value of the heat capacity lies between two previous experimental estimates. Our value of V_0 is very similar to that (57.9 cm^3/mol) found by Lacks et al. (2007) using empirical potentials. However, with compression their computed pressure deviates system-

Table 1
Equation of state fit parameters for Eqs. (4)–(13)

	Mg$_2$SiO$_4$ liquid	Forsterite
T_0 (K)	3000	1000
V_0 (cm^3/mol)	57.8 (3)	44.8 (2)
K_0 (GPa)	19 (3)	101 (7)
K_0'	6.2 (5)	5.4 (7)
C_V (V_X) (Nk_B)	4.29 (3)	3.10 (2)
C_V'	0.68 (16)	0.05 (8)
$\gamma(V_X)$	0.64 (6)	1.4 (2)
γ'	−1.2 (2)	1.8 (1.2)

Table 2
Comparison of liquid equation of state to experimental data, at $T = 2163$ K and $P = 0$ GPa (except heat capacity values, refer to references in footnote)

	LDA	Experiment
V_0 (cm^3/mol)	53.55	53.5 (2)[a]
		52.4 (2)[b]
K_0 (GPa)	23 (8)	9.5 (4)[b]
		24.3 (1)[c]
		27(1)[d,*]
		59[e]
K_0'	7 (1)	3.75[e]
		6.9[f,†]
α (10^{-6} K^{-1})	121 (50)	122 (7)[a]
		105 (5)[b]
C_V (Nk_B)	4.4 (5)	3.7 (4)[b,g,‡]
		4.9 (3)[b,h,◇]
γ	0.6 (1)	0.22 (4)[a,b,h]
		0.56 (3)[a,c,h]
		0.74 (4)[a,c,g]

[a]Lange (1997); [b]Lange and Carmichael (1987); [c]Ai and Lange (in press); [d]Rivers and Carmichael (1987) (*K_S); [e]Bottinga (1985); [f]Rigden et al. (1989); (†K_0' for CaMgSi$_2$O$_6$ liquid); [g]Tangeman et al. (2001) (‡Supercooled liquid at 1040–1773 K); [h]Stebbins et al. (1984) (◇1200–1850 K.)

Table 3
Comparison of crystalline equation of state with experimental values computed from the model of Stixrude and Lithgow-Bertelloni (2005) at $T = 1000$ K and $P = 0$ GPa

	LDA	Experiment
V_0 (cm^3/mol)	44.8 (2)	44.5
K_0 (GPa)	101 (7)	113.4 (2)
K_0'	5.4 (7)	4.6 (2)
α (10^{-6} K^{-1})	44 (10)	35 (1)
C_V (Nk_B)	3.10 (3)	2.92 (3)
γ	1.1 (3)	1.0 (3)

atically and increasingly from our predictions, being 1.4 GPa less at the smallest volume of their study (33.5 cm^3/mol) and 3000 K.

We find that liquid state isotherms diverge upon compression: the thermal pressure coefficient $B = \left(\frac{\partial P}{\partial T}\right)_V = \frac{\gamma C_V}{V}$ increases as the volume decreases. The isochoric heat capacity decreases from 4.4Nk_B at $V/V_X = 1.0$–3.7Nk_B at $V/V_X = 0.5$, and the Grüneisen parameter of the liquid increases from 0.6 to 1.2 over the same range of compression (Fig. 3), in contrast to the behavior of crystalline forsterite

for which C_V remains essentially constant at a value of about $3.1Nk_B$ and the Grüneisen parameter decreases on compression. Along the 3000 K isotherm, the enthalpy difference between liquid and solid decreases steadily, while the difference in volume reveals a density crossover at 16 ± 3 GPa (Fig. 2, inset). The pressure of the density crossover decreases with decreasing temperature.

3.2. Melting curve

We find that the melting temperature reaches a maximum of $T = 2550$ K at $P = 13$ GPa, well within the forsterite stability field (Akaogi et al., 1989), and has a negative slope at higher pressures as a result of a density crossover (Fig. 4). The entropy and volume of fusion at ambient conditions ($\Delta H/T_M = 0.95 \pm 0.04Nk_B$, $\Delta V = 5.7 \pm 0.1$ cm³/mol) agree with experimental estimates ($\Delta H/T_M = 0.91 \pm 0.16Nk_B$, Navrotsky et al., 1989; $\Delta V = 5.2 \pm 0.6$ cm³/mol, Lange and Carmichael, 1987, Lange, 1997). The entropy of fusion ($\Delta H/T_M$) along the melting curve decreases to $0.75Nk_B$ at 20 GPa, significantly lower than the entropy of melting of $MgSiO_3$ perovskite ($\sim 1.5Nk_B$) found in a previous simulation study (Stixrude and Karki, 2005).
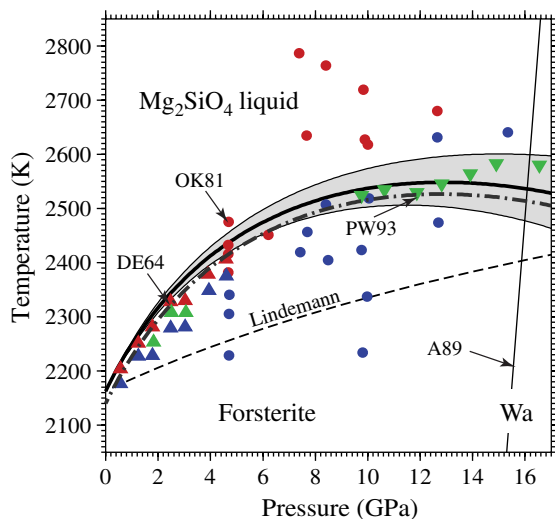

Fig. 4. FPMD melting curve for forsterite, obtained by integrating the Clausius–Clapeyron equation, with the 0 GPa experimental melting point of $T_{M_0} = 2163$ K (thick black line) or $T_{M_0} = 2140$ K (thick dot-dashed line) as integration constant. The gray envelope on either side of the 2163 K melting curve is based on integration with the upper and lower bounds of uncertainty in volume and enthalpy (see text). The slope becomes negative around 13 GPa due to a density crossover of the liquid relative to stable forsterite. Experimental data of Ohtani and Kumazawa (1981) (OK81; circles), Presnall and Walter (1993) (PW93; inverted triangles), Davis and England (1964) (DE64; triangles) are shown for observations of liquid (red symbols), crystal (blue symbols) and liquid–crystal coexistence (green symbols). The forsterite–wadsleyite (Wa) transition (thin black line) is from Akaogi et al. (1989) (A89). The Lindemann law melting curve obtained from the root mean square displacement $\langle u_{rms} \rangle$ in solid forsterite is also shown (dashed line). (For interpretation of the references to color in this figure legend, the reader is referred to the web version of this paper.)
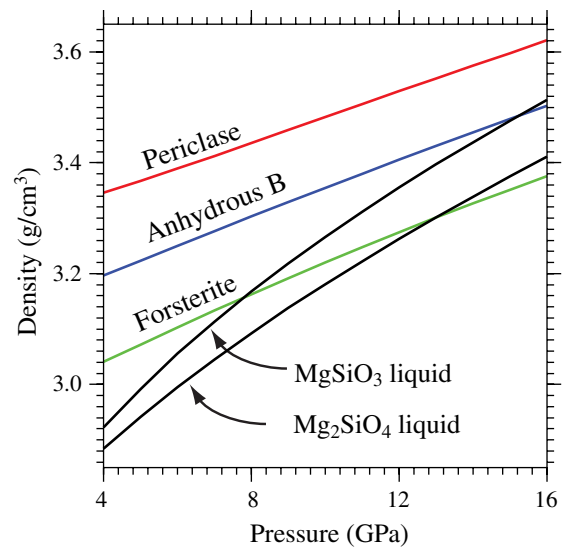

Fig. 5. Density contrast expected during incongruent melting of forsterite along the calculated melting curve (Fig. 4), between Mg_2SiO_4 and $MgSiO_3$ liquids and the phases that will comprise the residual crystalline assemblage (Presnall and Gasparik, 1990). The density of anhydrous B is estimated by ideal mixing of periclase (Karki et al., 2000) and forsterite.

Experimentally determined melting curves of forsterite disagree with one another above 10 GPa (Ohtani and Kumazawa, 1981; Presnall and Walter, 1993). At high pressures, our melting curve is in excellent agreement with the measurements of Presnall and Walter (1993), while at lower pressures it is slightly higher than the experimental measurements of both Davis and England (1964) and Ohtani and Kumazawa (1981).

Experimental evidence shows that, towards the high pressure end of the forsterite stability field, forsterite melts incongruently to a more silica-rich liquid (Ohtani and Kumazawa, 1981; Kato and Kumazawa, 1985; Presnall and Gasparik, 1990) and either anhydrous B or periclase. Fig. 5 illustrates that a more silica-rich liquid is denser than both forsterite and Mg_2SiO_4 liquid, though less dense than crystalline anhydrous B and periclase (Karki et al., 2000). Therefore partial melting of forsterite at high-pressure produces a liquid denser than crystalline forsterite. The liquidus phases on Mg_2SiO_4 composition at the base of the upper mantle (periclase and anhydrous B) are denser than the liquid.

The mean $\langle u_{rms} \rangle$ in forsterite varies between 0.05 Å² at 1000 K and 0.3 Å² at 3000 K, with a weak volume dependence of about 0.0065 Å² mol cm⁻³. Our Lindemann melting curve computed from interpolated values of $\langle u_{rms} \rangle$ (Fig. 4), shows poor agreement with experimental data and fails to capture the slope as well as its change with pressure (curvature) seen in both our FPMD results as well as the experimental data (Presnall and Walter, 1993).

3.3. Mg_2SiO_4 Hugoniot

We compare our theoretical Hugoniot for Mg_2SiO_4 liquid, together with Hugoniots for a partially molten sample

of periclase + MgSiO$_3$ liquid (Stixrude and Karki, 2005), and solid phase assemblages perovskite + periclase (Pv + Pe), post-perovskite + periclase (PPv + Pe) and stishovite + periclase (St + Pe) (Stixrude and Lithgow-Bertelloni, 2005), to the published high-pressure shock data for forsterite and wadsleyite (Jackson and Ahrens, 1979; Watt and Ahrens, 1983; Brown et al., 1987a,b; Luo et al., 2004; Mosenfelder et al., 2007) (Fig. 6).

Pressure–density and temperature measurements on the forsterite Hugoniot agree well with our computed Hugoniots of the sub-solidus assemblage (PPv + Pe) at pressures below 150 GPa, a mixture of periclase and

MgSiO$_3$ liquid between 150 and 170 GPa, and with pure Mg$_2$SiO$_4$ liquid at higher pressures. We find that the pressure–volume relation on the wadsleyite Hugoniot (there are no temperature measurements) is consistent with the sub-solidus assemblage at 140 GPa, and pure liquid or a mixture of periclase and MgSiO$_3$ liquid at 200 GPa. Shot #349 on wadsleyite is not consistent with any of our computed Hugoniots. The discrepancy with Mg$_2$SiO$_4$ liquid for wadsleyite shot #349 (almost 50 GPa) is much larger than the uncertainty in the simulated pressure (1.4 GPa), which includes the uncertainty estimates for P_{Pulay} and P_{emp} (Eq. (1)).
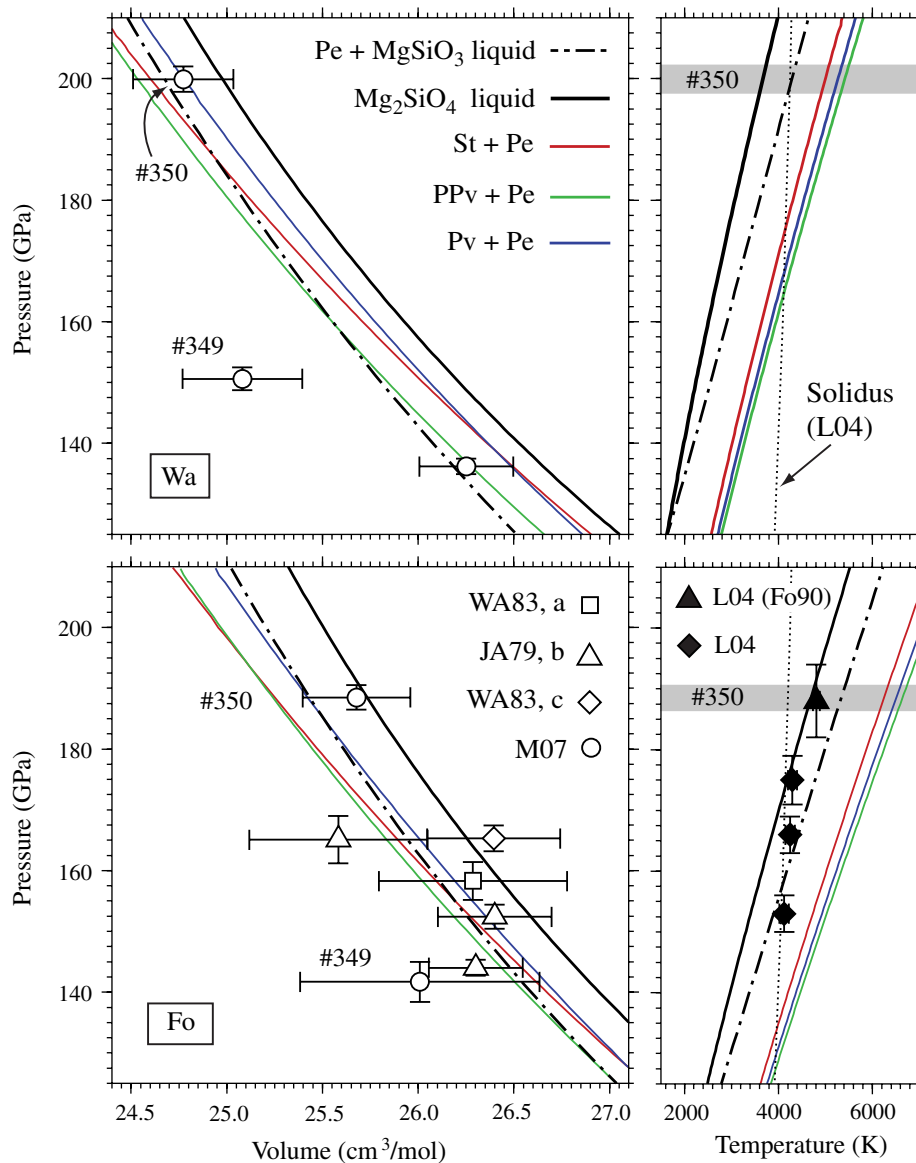

Fig. 6. Hugoniot curves calculated using the thermodynamic model of Stixrude and Lithgow-Bertelloni (2005) for crystalline phase assemblages (Pv, perovskite; PPv, post-perovskite; Pe, periclase; St, stishovite), as well as Mg$_2$SiO$_4$ liquid (this study) and a partially molten mixture of Pe and MgSiO$_3$ liquid (Stixrude and Karki, 2005), compared to the pressure-volume shock measurements for forsterite (Fo) and wadsleyite (Wa) (WA83, Watt and Ahrens, 1983; JA79, Jackson and Ahrens, 1979; M07, Mosenfelder et al., 2007), and to pressure–temperature shock measurements of forsterite and olivine (Fo90) (Luo et al., 2004). Data point labels refer to the shot numbers assigned by Mosenfelder et al. (2007).

3.4. Liquid structure

We define the bond length as the mode of the first peak in the partial radial distribution function (RDF) (McQuarrie, 2000). Upon compression, the Si–O bond length increases initially from a value of 1.63 Å (Fig. 8) to 1.64 Å at $V/V_X = 0.7$ and then decreases to 1.62 Å at 3000 K and the highest compression considered. Over the same compression interval the Mg–O bond length decreases from 1.97 to 1.83 Å. The mode and median of the first peak diverge, as the radial distribution function broadens with increasing distortion of the polyhedra on compression. Si–O and Mg–O bond lengths and coordination numbers at low pressure compare very well with experimental data (Kohara et al., 2004) on the structure of Mg_2SiO_4 glasses (Table 4).

The coordination number ($Z_{\alpha\beta}$) is computed as the integral of the radial distribution function $g_{\alpha\beta}(r)$

$$Z_{\alpha\beta} = 4\pi\rho \int_0^{r_{cut}} g_{\alpha\beta}(r) r^2 \, dr, \tag{22}$$

Table 4
Comparison of simulated liquid structure to experimental data (Kohara et al., 2004)

	LDA ($V/V_X = 1.0$; $T = 3000$ K)	Experiment ($P = 0$GPa; $T = 300$ K glass)
$d_{Mg–O}$	1.97 Å	2.00 Å
$d_{Si–O}$	1.63 Å	1.63 Å
$Z_{Mg–O}$	5.1	5.0
$Z_{Si–O}$	4.1	4.1
$_{[4]}Si^0$	22%	∼ 50%
$_{[4]}Si^1$	38%	∼ 50%
$_{[4]}Si^2$	21%	—
$_{[4]}Si^3$	10%	—

where ρ is the density and r_{cut} is the position of the first minimum in $g_{\alpha\beta}$. $Z_{Si–O}$ increases from 4.1 to 6.0, while $Z_{Mg–O}$ increases from 5.1 to 7.7 (Fig. 7) on twofold compression. The smooth and nearly linear increase on compression is facilitated by gradual changes in the abundances of the various coordination species, of which a mixture is present at all conditions studied (Fig. 8). The variety of local coordination environments may also be characterized by the O–Si coordination number ($Z_{O–Si}$), which shows relative abundances changing upon compression (Fig. 9). At low pressure, the liquid has ∼15% (or 0.6 O per Si) bridging oxygens (O_B; $Z_{O–Si} = 2$) and ∼70% (2.8 O per Si) non-bridging oxygens (O_N; $Z_{O–Si} = 1$). The remaining 15% of O atoms are not bound to Si (O_F; $Z_{O–Si} = 0$), and are hence referred to as 'free oxygens' (Hess, 1980) (red spheres in Fig. 1). Changes in the concentrations of the various O and Si coordination species with pressure are associated with increased polymerization and Si coordination.

Analysis of atomic trajectories reveals that coordination increases through the following two reactions:

$$O_N + _{[Z]}Si^{O_B} \quad \leftrightarrow \quad _{[Z+1]}Si^{O_B+1}, \tag{23}$$

$$O_F + _{[Z]}Si^{O_B} \quad \leftrightarrow \quad _{[Z+1]}Si^{O_B}. \tag{24}$$

We describe the local structure about Si atoms as $_{[Z]}Si^{O_B}$, with [Z] the coordination number and O_B the number of bridging oxygens. Our notation is a generalization of the commonly used Q^{O_B} notation, which specifies the number of bridging oxygens in systems for which $Z = 4$. Reactions (23) and (24) are illustrated by the increase in the proportion of bridging oxygens as the proportion of free oxygens decreases on compression (Fig. 9). Bridging oxygens are almost never added to the coordination shell of another silicon and therefore do not contribute significantly to the coordination increase, consistent with Raman, infrared,
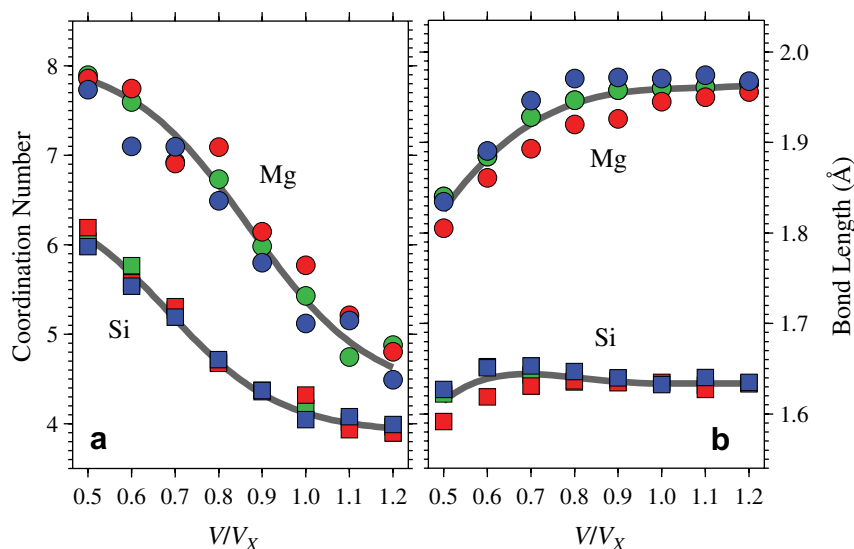

Fig. 7. (a) $Z_{Si–O}$ (squares) and $Z_{Mg–O}$ (circles) increase continuously as a function of volume. (b) Si–O bond lengths initially increase on compression whereas Mg–O bond lengths decrease monotonically. Temperature is indicated by the color of the symbols: 3000 K (blue), 4000 K (green) and 6000 K (red). (For interpretation of the references to color in this figure legend, the reader is referred to the web version of this paper.)
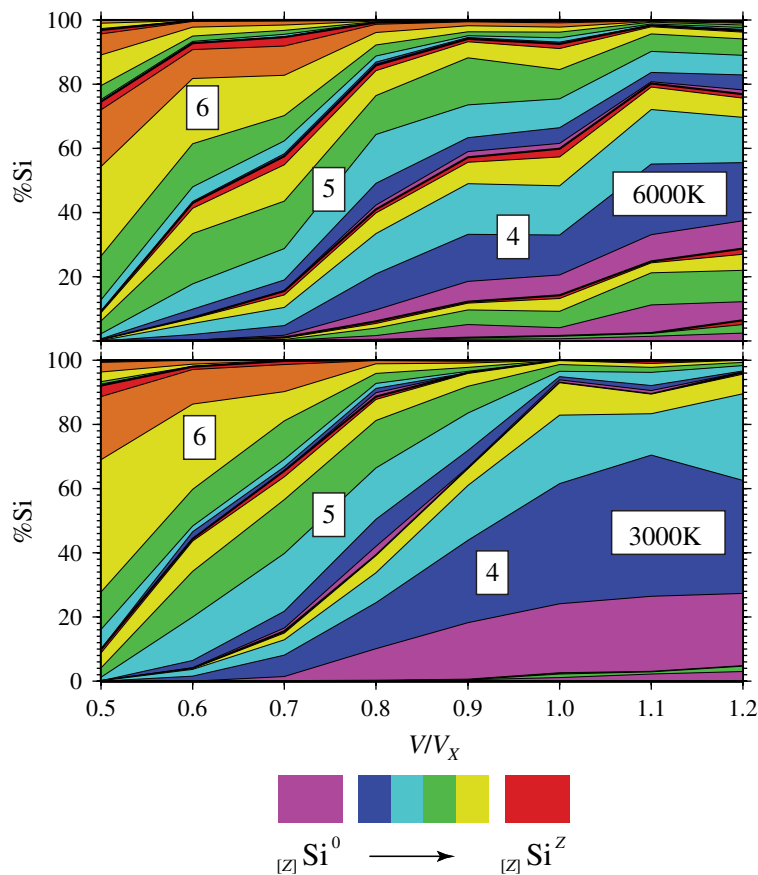
Fig. 8. Polymerization state of the liquid as a function of volume, at 3000 K and 6000 K, as expressed by the abundance of $_{[Z]}$Si^{O_B} species. Colors cycle from purple ($_{[Z]}$Si^0; zero bridging oxygens) to red ($_{[Z]}$Si^Z; all oxygens are bridging) with the number of intermediate colors depending on the coordination number. Coordination 'zones' result as the mean coordination number increases with compression. At 3000 K, low-pressure liquids are almost entirely fourfold coordinated, with the majority of polyhedra free-floating (purple) or bound in dimers (dark blue). The liquid moves through intermediate states and fivefold coordination upon compression, reaching almost entirely sixfold coordination at the highest compression, where the majority of polyhedra have only one or two non-bridging oxygens. (For interpretation of the references to color in this figure legend, the reader is referred to the web version of this paper.)

and nuclear magnetic resonance spectroscopic observations in alkali-silicate glasses (Wolf et al., 1990; Xue et al., 1991) showing coordination increases primarily at the expense of non-bridging oxygens. Examples of reactions (23) and (24) are illustrated in Fig. 10 in which $_{[4]}$Si^1 is shown transforming into $_{[4]}$Si^0 (top panel), and $_{[4]}$Si^3 to $_{[3]}$Si^2 and then to $_{[5]}$Si^4 (bottom panel).

3.5. Transport properties

Characteristic bond lifetimes calculated from the bond breaking rate (Kubicki and Lasaga, 1991) reveal a strong decrease in the average Si–O bond lifetime from 2000 fs at ambient pressure and 3000 K to 500 fs at high-pressure. Mg–O bond lifetimes increase only slightly over the same pressure range from 300 to 400 fs. Over the same compression range, the long lifetimes of O$_F$ and O$_N$ at low pressure (~1500 fs at 3000 K) decrease to values similar to that of O$_B$ (500 fs at 3000 K) which remain essentially unchanged as a function of volume.

Self-diffusion coefficients increase with temperature and decrease with pressure (Fig. 12), and do not show the initial increase with increasing pressure seen in more highly polymerized silicate liquids (Angell et al., 1982; Karki et al., 2007): The pressure and temperature dependence is well described by the Arrhenius relation. Fit parameters for Mg, Si, O and total self-diffusion (Table 5) are found to be independent of temperature over the range investigated.

By comparing with longer runs, we find 2400 ergodic timesteps to be sufficient to determine robust values of the self-diffusion coefficient values from the mean square displacement $\langle [r(t)]^2 \rangle$ (Fig. 11), for all simulations except the $V/V_X = 0.5$; $T = 4000$ K and $V/V_X = 0.6$; $T = 3000$ K points, for which 5000 timesteps are sufficient. The $V/V_X = 0.5$; $T = 3000$ K point is not included in the analysis of thermodynamic and transport properties, because we find it to be a glass: $\langle [r(t)]^2 \rangle$ flattens out at 0.25 Å^2, similar to values found in the solid at low pressure, though somewhat higher than solid values extrapolated to $V/V_X = 0.5$ (0.17 Å^2).

Eq. (20) implies a $N^{-1/3}$ dependence of diffusivity on system size. The corrected total diffusivity at $V/V_X = 1.0$; $T = 3000$ K, ($D_\infty = 6.13 \pm 0.6 \times 10^{-9}$ m^2/s) calculated with Eq. (20) is similar to the value ($D_\infty = 6.7 \pm 0.7 \times 10^{-9}$ m^2/s) we find from the linear relation
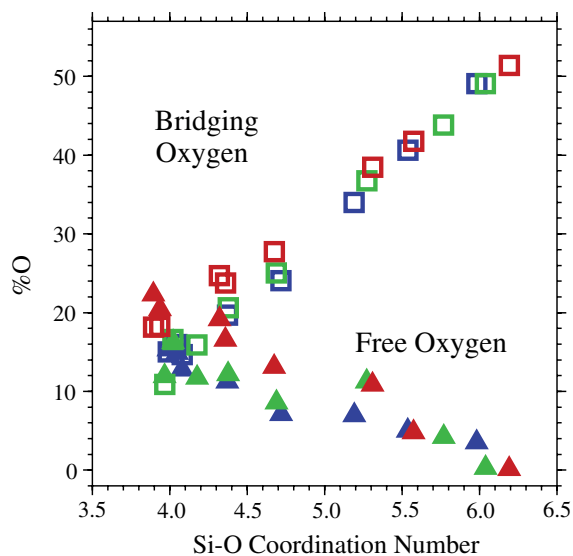
Fig. 9. As Z_{Si-O} increases with compression, the abundance of free oxygen (O_F) decreases while that of bridging oxygen (O_B) increases. Note that $\|\partial O_B/\partial Z\| > \|\partial O_F/\partial Z\|$, indicating that coordination increase occurs more frequently through the transformation of a non-bridging oxygen (O_N) into a O_B, compared to a O_F transforming to a O_N.

Table 5
Self-diffusion coefficient Arrhenius relation (Eq. (19)) fit parameters

	D_∞^0 (10^{-9} m^2/s)	D_N^0 (10^{-9} m^2/s)	E_a (kJ/ mol)	V_a (cm^3/ mol)
Total	485 (70)	339 (49)	106 (5)	0.88 (7)
Si	476 (108)	332 (76)	124 (8)	0.76 (9)
Mg	359 (69)	251 (48)	87 (6)	1.00 (7)
O	560 (85)	391 (59)	113 (6)	0.87 (8)

$$D_N = D_\infty + aN^{-1/3} \qquad (25)$$

fit to our results for 112 and 336 atoms.

4. DISCUSSION

The structure of Mg_2SiO_4 liquid differs markedly from that of crystalline forsterite. Whereas in forsterite all O are bound to Si, with SiO_4 tetrahedra isolated from one another (entirely Q^0 or $_{[4]}Si^0$ in our notation), in the liquid free oxygens and tetrahedral linkages ($Q^{\geqslant 1}$ or $_{[4]}Si^{\geqslant 1}$) appear. Free oxygens are also present in the high-pressure crystalline polymorph wadsleyite, in which all tetrahedra exist as dimers (Si_2O_7). The difference in structure between Mg_2SiO_4 liquid and forsterite is important as it accounts for the very large enthalpy of vitrification of Mg_2SiO_4
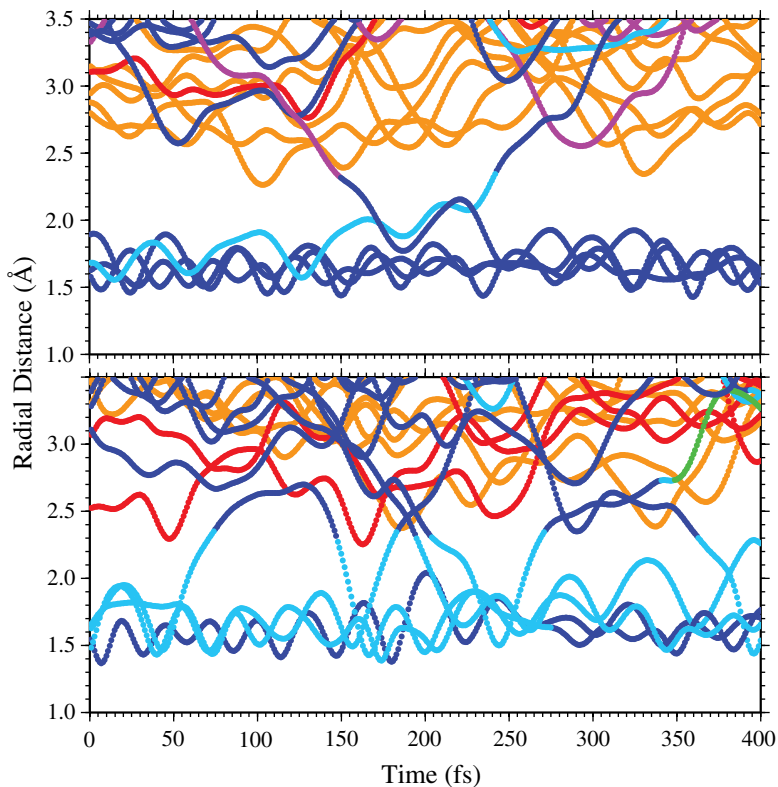

Fig. 10. Time dependence of the movement of atoms within a 3.5 Å sphere around a reference silicon atom (at 0 Å), illustrates dynamic speciation changes. Each trace represents a single atom, with speciation indicated by the color: free oxygen, purple; non-bridging oxygen, navy blue; bridging oxygen, light blue; three coordinated oxygen, green; magnesium, orange; silicon, red. In the top panel a free oxygen approaches the reference silicon eventually binding with it to become a non-bridging oxygen (Eq. (24)). Coincident with this process a bridging oxygen moves away from the reference silicon, eventually losing its bond to become non-bridging (bound to a different silicon) (reverse of Eq. (23)). The bottom panel shows a number of events where oxygen atoms transform between bridging and non-bridging. Also note the coupled movement of the silicon atom at around $t = 160$ fs, as it exchanges oxygens with the reference silicon. (For interpretation of the references to color in this figure legend, the reader is referred to the web version of this paper.)
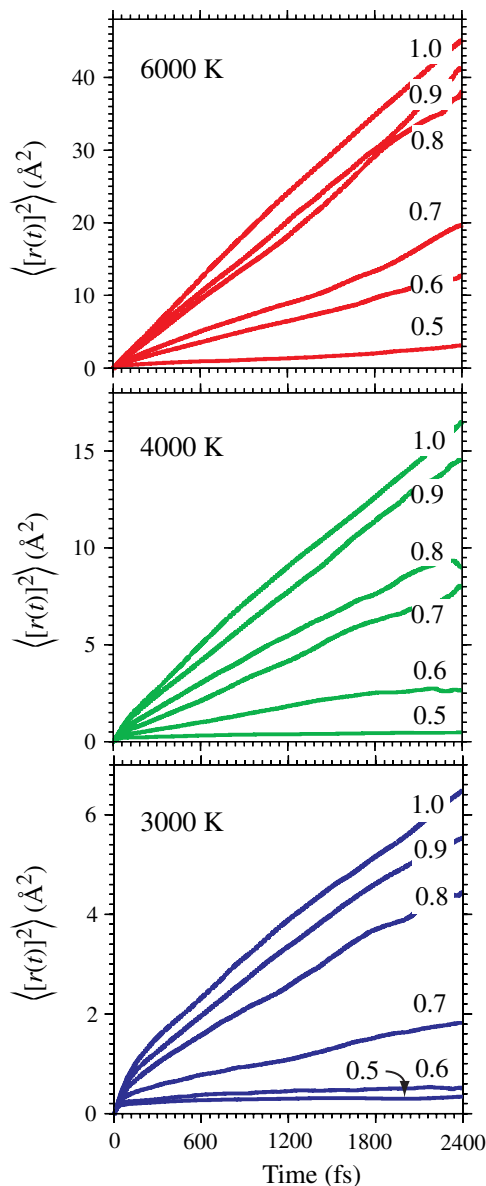
Fig. 11. Mean square displacement values of atoms in the simulations increases with a constant slope after ~100 fs, from which the diffusivity is calculated through Eq. (18).

(Kohara et al., 2004) and the failure of the Lindemann law in this system. Evidence of dimers in amorphous Mg$_2$SiO$_4$ had previously been obtained only for the glass, via vibrational spectroscopy, nuclear magnetic resonance, and X-ray diffraction (McMillan, 1984; Williams et al., 1989; Cooney and Sharma, 1990; Williams, 1990; Kohara et al., 2004). While experimental studies have found evidence only for Q^0 and Q^1 species, we also find a substantial number of Q^2 and Q^3. We find that the abundance of Q^2 and Q^3 species decreases with decreasing temperature so that they may not be detectable in the glass. The liquid also differs from the structure of crystalline phases in having $Z_{Mg-O} = 5.1$, substantially less than that in the tetrahedrally coordinated crystalline polymorphs ($Z_{Mg-O} = 6$), which accounts for the volume of melting.

The structure of the liquid remains distinct from that of crystalline phases at elevated pressure. The Si–O (and Mg–O) coordination number of the liquid increases monotonically with compression over the entire range studied, in sharp contrast to that of the crystalline phases in which the coordination number remains $Z_{Si-O} = 4$ up to the transformation of ringwoodite to perovskite and periclase near 24 GPa, where it increases to $Z_{Si-O} = 6$. Liquid structure is also distinct in that it shows an initial increase in Si–O bond length on compression, which we attribute to the increase in coordination number.

We suggest an alternative interpretation of the dynamic compression of forsterite that is consistent with our computed Hugoniots, the shock temperature measurements of Luo et al. (2004) and the pressure–volume data of Mosenfelder et al. (2007) except the wadsleyite portion of shot #349. Dynamic loading of forsterite produces incongruent melting to periclase and a more silica-rich liquid at 150–170 GPa. At higher pressures, pure Mg$_2$SiO$_4$ liquid is present on the forsterite Hugoniot, while at lower pressures, sub-solidus assemblages (PPv + Pe) are present on the Hugoniot.

This picture has important implications for the interpretation of the wadsleyite Hugoniot (Mosenfelder et al., 2007) and of sound speed data (Brown et al., 1987a,b). We find the wadsleyite Hugoniot to be 1000–1400 K colder than that of forsterite at 150–200 GPa. It is therefore likely that even the highest pressure wadsleyite point of Mosenfelder et al. (2007) (shot #350) is either sub-solidus or only partially molten. We therefore suggest that determination of a liquid phase value of the Grüneisen parameter based on these data should be treated with caution. While Mosenfelder et al. (2007) find that the Grüneisen parameter increases on compression in the liquid, in general agreement with the trend that we find, their value (2.6) is much higher than our predictions. This discrepancy is explained if the measured portion of the wadsleyite Hugoniot is less than completely molten. Our interpretation cannot account for shot #349 on wadsleyite of Mosenfelder et al. (2007) which lies at much lower pressures than all our computed Hugoniots. Sound speed measurements have been interpreted to indicate melting on the forsterite Hugoniot above 150 GPa. The measured value of the sound speed at 168 GPa (10.8 km/s) is considerably less than what we find at the same pressure: 11.5 km/s varying little with temperature from 3000 to 6000 K. The smaller experimental value may be due to incongruent melting: a solid–liquid mixture with proportions varying as the shock front passes. Because the experimental sample may be only partially molten, the value of the Grüneisen parameter determined (2.1), which is substantially higher than our predicted value, may not be representative of the liquid state. Indeed, at higher pressures (195 GPa) the experimental sound velocity (12.2 km/s Brown et al., 1987a) agrees well with extrapolation of our results (12.4 ± 0.2 km/s), consistent with complete melting in the shocked sample.

The behavior of the Grüneisen parameter that we calculate in the liquid—increasing on compression—is contrary to that of all mantle crystalline phases, for which the

Grüneisen parameter decreases with compression (Fig. 3). This behavior was first recognized in silicate liquids by Stixrude and Karki (2005), and has also been found in studies of non-silicate liquids (Davis and Gordon, 1967; Knopoff and Shapiro, 1970; Boehler and Kennedy, 1977; Vocadlo et al., 2003; Karki et al., 2006). The increase of the Grüneisen parameter on compression in the liquid can be understood as follows. While γ decreases with compression in crystalline phases, it increases across pressure induced phase transitions associated with an increase in Si coordination (Jeanloz and Roufosse, 1982) (Fig. 3). Since the coordination number increases gradually and continuously in the liquid, we expect the Grüneisen parameter also to increase on compression as it adopts values characteristic of higher coordinated states.

Increasing coordination is further expressed as a density crossover, providing fundamental insight into the contrasting behavior of complex liquids and solids upon compression. Our results reveal the origin of olivine flotation in compositions thought to be representative of an initial magma ocean (Stolper et al., 1981; Agee and Walker, 1988; Ohtani, 1988; Trønnes and Frost, 2002). The density crossover originates primarily in the structure of the liquid and occurs, even in forsterite composition, at 13 GPa along the solidus, where the Si–O coordination number of the liquid is 4.4, greater than that in the crystal. In natural compositions the density of the liquid will be further enhanced relative to that of coexisting solids by the incompatibility of abundant heavy elements, such as Fe and Ca. The isochemical density crossover that we find supports the notion that buoyantly stable silicate melt may exist at the base of the

olivine stability field in the mantle at 410 km depth (Revenaugh and Sipkin, 1994).

The discrepancy between our melting curve and experimental data at low pressures may be related to uncertainty in the ambient melting point of forsterite. To illustrate, also shown in Fig. 4 is an alternative melting curve obtained by using $T_{M_0} = 2140$ K, which represents the lower bound of the quoted uncertainty for the ambient melting temperature determined by Bowen and Andersen (1914). Integration of the Clausius–Clapeyron Eq. (14) based on our results and this value of T_{M_0} improves agreement with the data of Davis and England (1964), while maintaining agreement at high pressure with the data of Presnall and Walter (1993).

The failure of the Lindemann law to capture the change in slope of the melting curve with pressure is not surprising, since it assumes that the structure of the liquid remains constant along the melting curve (Ross, 1969). The changes in liquid structure that we find reduce the volume of the liquid relative to the Lindemann picture, causing the melting slope to decrease rapidly with pressure. We thus reinforce the overall conclusion of Wolf and Jeanloz (1984) that the Lindemann criterion should not be used to extrapolate melting temperatures of mantle phases, although those authors found good agreement in the case of forsterite between the Lindemann law and the data of Ohtani and Kumazawa (1981), in notable contrast to other minerals considered in their study, and with our findings.

The short lifetime of the Mg–O bond relative to that of the Si–O bond is consistent with the smaller activation energy and higher self-diffusion coefficients found for Mg compared to Si (Table 5). While our activation energy values are similar
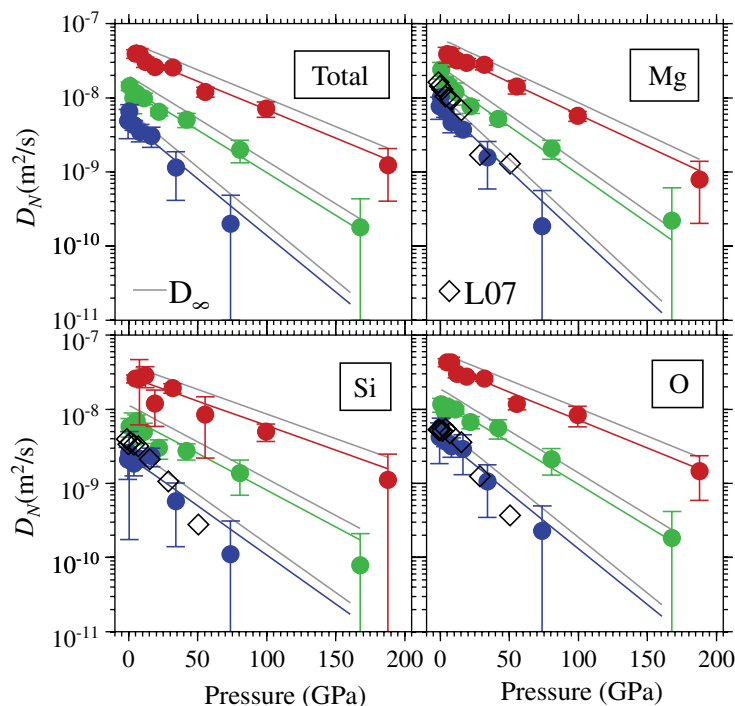

Fig. 12. Self-diffusion coefficient (D_N) of Mg_2SiO_4 liquid, fit with an Arrhenius relation (Eq. (19)). Fit parameters are reported in Table 5. Gray lines indicate the Arrhenius fit to diffusivities corrected for finite system size through Eqs. (20) and (21). Open diamonds show the empirical potential calculation results of Lacks et al. (2007) (L07).

to those obtained by Kubicki and Lasaga (1991), our finite size-corrected self-diffusion coefficients are much larger. Conversely, our low-pressure self-diffusion coefficients are similar to results of Lacks et al. (2007), but the pressure dependence of their results implies a higher activation volume (Fig. 12). These previous simulations are based on semi-empirical interatomic potentials, and differences likely reflect uncertainties related to the construction of inter atomic force models in the earlier studies, emphasizing the importance of our parameter free first principles simulations. No experimental values of self-diffusion in forsterite liquid exist; data that have been obtained are on more silica-rich compositions. For example, the experimental value of the activation energy for diffusion of Silicon and Oxygen in CaMgSi$_2$O$_6$ melt (Kubicki et al., 1990; Reid et al., 2001), is much greater than our value for forsterite. This difference may reflect the difference in silica content, and therefore fragility (Angell, 1995) of forsterite versus diopside composition melts, as well as the lower temperature range over which the experimental value is obtained.

5. CONCLUSIONS

Our first principles molecular dynamics calculations for Mg$_2$SiO$_4$ liquid show the Grüneisen parameter and thermal pressure coefficient increasing upon compression. Comparison of the liquid equation of state to that which we calculate for forsterite shows the presence of a density crossover at pressures of 12–17 GPa and temperatures of 2000–3500 K. Along the melting curve we determine by integration of the Clausius–Clapeyron equation, the density crossover is found at 13 GPa, within the stability field of forsterite. Comparison of our melting curve to an extrapolation of the ambient melting temperature through the Lindemann law indicates that such extrapolations for silicates cannot yield accurate results, due to significant differences in structure between the liquid and the solid, and significant changes in liquid structure on compression, primarily expressed as a continuous increase in coordination and polymerization. Comparison of the liquid equation of state to the available high-pressure shock wave data is consistent with partial melting along the forsterite Hugoniot at pressures above 150 GPa, and complete melting at pressures above 170 GPa; and sub-liquidus conditions on the wadsleyite Hugoniot up to the highest pressures measured to date (200 GPa). Liquid diffusivities increase with temperature and decrease monotonically with pressure, and are found to be well described by the Arrhenian relation.

REFERENCES

Agee C. B. and Walker D. (1988) Static compression and olivine flotation in ultrabasic silicate liquid. *J. Geophys. Res.* **93**, 3437–3449.

Ai Y. and Lange R. A. (in press) The compressibility of CaO–MgO–Al$_2$O$_3$–SiO$_2$ liquids from new acoustic velocity measurements: reevaluation of the equation of state of CaMgSi$_2$O$_6$–CaAl$_2$SiO$_8$ liquids to 25 GPa. *J. Geophys. Res.*

Akaogi M., Ito E. and Navrotsky A. (1989) Olivine-modified spinel–spinel transitions in the system Mg$_2$SiO$_4$–Fe$_2$SiO$_4$—calorimetric measurements, thermochemical calculation, and geophysical application. *J. Geophys. Res.* **94**, 15671–15685.

Alfe D. (2005) Melting curve of MgO from first-principles simulations. *Phys. Rev. Lett.* **94**, 235701.

Angell C. A. (1995) Formation of glasses from liquids and biopolymers. *Science* **267**, 1924–1935.

Angell C. A., Cheeseman P. A. and Tamaddon S. (1982) Pressure enhancement of ion mobilities in liquid silicates from computer-simulation studies to 800-Kilobars. *Science* **218**, 885–887.

Birch F. (1952) Elasticity and constitution of the Earth's interior. *J. Geophys. Res.* **57**, 227–286.

Boehler R. and Kennedy G. C. (1977) Pressure-dependence of thermodynamical Grüneisen parameter of fluids. *J. Appl. Phys.* **48**, 4183–4186.

Bottinga Y. (1985) On the isothermal compressibility of silicate liquids at high-pressure. *Earth Planet. Sci. Lett.* **74**, 350–360.

Bowen N. L. and Andersen O. (1914) The binary system MgO–SiO$_2$. *Am. J. Sci.* **37**, 487–500.

Brown J. M., Furnish M. D. and Boness D. A. (1987a) Sound velocities for San Carlos olivine. In *Shock Waves in Condensed Matter* (eds. S. C. Schmidt and N. C. Holmes). Elsevier, Amsterdam.

Brown J. M., Furnish M. D. and McQueen R. G. (1987b) Thermodynamics for (Mg,Fe)$_2$SiO$_4$ from the Hugoniot. In *High-Pressure Research in Mineral Physics* (eds. M. H. Manghnani and Y. Syono). American Geophysical Union, Washington, DC.

Ceperley D. M. and Alder B. J. (1980) Ground-state of the electron-gas by a stochastic method. *Phys. Rev. Lett.* **45**, 566–569.

Cooney T. F. and Sharma S. K. (1990) Structure of glasses in the systems Mg$_2$SiO$_4$–Fe$_2$SiO$_4$, Mn$_2$SiO$_4$–Fe$_2$SiO$_4$, Mg$_2$SiO$_4$–CaMgSiO$_4$, and Mn$_2$SiO$_4$–CaMnSiO$_4$. *J. Non-Cryst. Solids* **122**, 10–32.

Davis B. T. C. and England J. L. (1964) Melting of forsterite up to 50 kilobars. *J. Geophys. Res.* **69**, 1113–1116.

Davis L. A. and Gordon R. B. (1967) Compression of mercury at high pressure. *J. Chem. Phys.* **46**, 2650.

Flyvberg H. and Petersen H. G. (1989) Error-estimates on averages of correlated data. *J. Chem. Phys.* **91**, 461–466.

Francis G. P. and Payne M. C. (1990) Finite basis set corrections to total energy pseudopotential calculations. *J. Phys. Condens. Matter* **2**, 4395–4404.

Garnero E. J. and Helmberger D. V. (1995) A very slow basal layer underlying large-scale low-velocity anomalies in the lower mantle beneath the Pacific: evidence from core phases. *Phys. Earth Planet. Interiors* **91**, 161–176.

Gillan M. J., Alfe D., Brodholt J. P., Vocadlo L. and Price G. D. (2006) First-principles modelling of Earth and planetary materials at high pressures and temperatures. *Rep. Prog. Phys.* **69**, 2365–2441.

Gilvarry J. J. (1956) The Lindemann and Grüneisen Laws. *Phys. Rev.* **102**, 308–316.

Gomes Dacosta P., Nielsen O. H. and Kunc K. (1986) Stress theorem in the determination of static equilibrium by the density functional method. *J. Phys. C: Solid State Phys.* **19**, 3163–3172.

Hess P. C. (1980) Polymerization model for silicate melts. In *Physics of Magmatic Processes* (ed. R. B. Hargraves). Princeton University Press, Princeton, NJ.

Hohenberg P. and Kohn W. (1964) Inhomogeneous electron gas. *Phys. Rev. B* **136**, B864.

Holland K. G. and Ahrens T. J. (1997) Melting of $(Mg,Fe)_2SiO_4$ at the core–mantle boundary of the Earth. *Science* **275**, 1623–1625.

Jackson I. and Ahrens T. J. (1979) Shock wave compression of single-crystal forsterite. *J. Geophys. Res.* **84**, 3039–3048.

Jeanloz R. and Roufosse M. (1982) Anharmonic properties—ionic model of the effects of compression and coordination change. *J. Geophys. Res.* **87**, 763–772.

Karki B. B., Wentzcovitch R. M., De Gironcoli S. and Baroni S. (2000) High-pressure lattice dynamics and thermoelasticity of MgO. *Phys. Rev. B* **61**, 8793–8800.

Karki B. B., Stixrude L. and Wentzcovitch R. M. (2001) High-pressure elastic properties of major materials of Earth's mantle from first principles. *Rev. Geophys.* **39**, 507–534.

Karki B. B., Bhattarai D. and Stixrude L. (2006) First principles calculations of the structural, dynamical and electronic properties of liquid MgO. *Phys. Rev. B* **73**, 174208.

Karki B. B., Bhattarai D. and Stixrude L. (2007) First-principles simulations of liquid silica: structural and dynamical behavior at high pressure. *Phys. Rev. B* **76**, 104205.

Kato T. and Kumazawa M. (1985) Effect of high-pressure on the melting relation in the system Mg_2SiO_4–$MgSiO_3$. 1. Eutectic relation up to 7 GPa. *J. Phys. Earth* **33**, 513–524.

Knopoff L. and Shapiro J. N. (1970) Pseudo-Grüneisen parameter of liquids. *Phys. Rev. B* **1**, 3893.

Kohara S., Suzuya K., Takeuchi K., Loong C. K., Grimsditch M., Weber J. K. R., Tangeman J. A. and Key T. S. (2004) Glass formation at the limit of insufficient network formers. *Science* **303**, 1649–1652.

Kohn W. and Sham L. J. (1965) Self-consistent equations including exchange and correlation effects. *Phys. Rev.* **140**, 1133.

Kresse G. and Furthmüller J. (1996) Efficiency of ab-initio total energy calculations for metals and semiconductors using a plane-wave basis set. *Comput. Mater. Sci.* **6**, 15–50.

Kresse G. and Hafner J. (1994) Norm-conserving and ultrasoft pseudopotentials for first-row and transition-elements. *J. Phys. Condens. Matter* **6**, 8245–8257.

Kubicki J. D. and Lasaga A. C. (1991) Molecular-dynamics simulations of pressure and temperature effects on $MgSiO_3$ and Mg_2SiO_4 melts and glasses. *Phys. Chem. Miner.* **17**, 661–673.

Kubicki J. D., Muncill G. E. and Lasaga A. C. (1990) Chemical diffusion in melts on the $CaMgSi_2O_6$–$CaAl_2Si_2O_8$ join under high-pressures. *Geochim. Cosmochim. Acta* **54**, 2709–2715.

Lacks D. J., Rear D. B. and Van Orman J. A. (2007) Molecular dynamics investigation of viscosity, chemical diffusivities and partial molar volumes of liquids along the MgO–SiO_2 join as functions of pressure. *Geochim. Cosmochim. Acta* **71**, 1312–1323.

Lange R. A. (1997) A revised model for the density and thermal expansivity of K_2O–Na_2O–CaO–MgO–Al_2O_3–SiO_2 liquids from 700 to 1900 K: extension to crustal magmatic temperatures. *Contrib. Mineral. Petrol.* **130**, 1–11.

Lange R. A. and Carmichael I. S. E. (1987) Densities of Na_2O–K_2O–CaO–MgO–FeO–Fe_2O_3–Al_2O_3–TiO_2–SiO_2 liquids—new measurements and derived partial molar properties. *Geochim. Cosmochim. Acta* **51**, 2931–2946.

Lange R. A. and Navrotsky A. (1992) Heat capacities of Fe_2O_3-bearing silicate liquids. *Contrib. Mineral. Petrol.* **110**, 311–320.

Lindemann F. A. (1910) Über die berechnung molekularer Eigenfrequenzen. *Phys. Z.* **11**, 609–612.

Luo S.-N., Akins J. A., Ahrens T. J. and Asimow P. D. (2004) Shock-compressed $MgSiO_3$ glass, enstatite, olivine, and quartz: optical emission, temperatures, and melting. *J. Geophys. Res.* **109**, B05205.

McMillan P. (1984) A Raman spectroscopic study of glasses in the system CaO–MgO–SiO_2. *Am. Mineral.* **69**, 645–659.

McQuarrie D. A. (2000) *Statistical Mechanics*. University Science Books, Mill Valley.

Monkhorst H. J. and Pack J. D. (1976) Special points for Brillouin-zone integrations. *Phys. Rev. B* **13**, 5188–5192.

Mosenfelder J. L., Asimow P. D. and Ahrens T. J. (2007) Thermodynamic properties of Mg_2SiO_4 liquid at ultra-high pressures from shock measurements to 200 GPa on forsterite and wadsleyite. *J. Geophys. Res.* **112**. doi:10.1029/2006JB004364.

Navrotsky A., Ziegler D., Oestrike R. and Maniar P. (1989) Calorimetry of silicate melts at 1773 K—measurement of enthalpies of fusion and of mixing in the systems diopside–anorthite–albite and anorthite–forsterite. *Contrib. Mineral. Petrol.* **101**, 122–130.

Nosé S. (1984) A unified formulation of the constant temperature molecular dynamics methods. *J. Chem. Phys.* **81**, 511–519.

Oganov A. R., Brodholt J. P. and Price G. D. (2001) The elastic constants of $MgSiO_3$ perovskite at pressures and temperatures of the Earth's mantle. *Nature* **411**, 934–937.

Ohtani E. (1988) Chemical stratification of the mantle formed by melting in the early stage of the terrestrial evolution. *Tectonophysics* **154**, 201–210.

Ohtani E. and Kumazawa M. (1981) Melting of Forsterite Mg_2SiO_4 up to 15 GPa. *Phys. Earth Planet. Interiors* **27**, 32–38.

Presnall D. C. and Gasparik T. (1990) Melting of enstatite $(MgSiO_3)$ from 10 to 16.5 GPa and the forsterite (Mg_2SiO_4)–majorite $(MgSiO_3)$ eutectic at 16.5 GPa: implications for the origin of the mantle. *J. Geophys. Res.* **95**, 15771–15777.

Presnall D. C. and Walter M. J. (1993) Melting of Forsterite, Mg_2SiO_4, from 9.7 to 16.5 GPa. *J. Geophys. Res.* **98**, 19777–19783.

Reid J. E., Poe B. T., Rubie D. C., Zotov N. and Wiedenbeck M. (2001) The self-diffusion of silicon and oxygen in diopside $(CaMgSi_2O_6)$ liquid up to 15 GPa. *Chem. Geol.* **174**, 77–86.

Revenaugh J. and Sipkin S. A. (1994) Seismic evidence for silicate melt atop the 410 km mantle discontinuity. *Nature* **369**, 474–476.

Rigden S. M., Ahrens T. J. and Stolper E. M. (1989) High-pressure equation of state of molten anorthite and diopside. *J. Geophys. Res.* **94**, 9508–9522.

Rivers M. L. and Carmichael I. S. E. (1987) Ultrasonic studies of silicate melts. *J. Geophys. Res.* **92**, 9247–9270.

Ross M. (1969) Generalized Lindemann melting law. *Phys. Rev.* **184**, 233–242.

Song T. R. A., Helmberger D. V. and Grand S. P. (2004) Low-velocity zone atop the 410-km seismic discontinuity in the northwestern United States. *Nature* **427**, 530–533.

Stebbins J. F., Carmichael I. S. E. and Moret L. K. (1984) Heat-capacities and entropies of silicate liquids and glasses. *Contrib. Mineral. Petrol.* **86**, 131–148.

Stixrude L. (2001) First principles theory of mantle and core phases. In *Molecular Modeling Theory: Applications in the Geosciences* (eds. R. T. Cygan and J. D. Kubicki). Geochemical Society and Mineralogical Society of America, Washington, DC.

Stixrude L. and Bukowinski M. S. T. (1990) Fundamental thermodynamic relations and silicate melting with implications for the constitution of the D''. *J. Geophys. Res.* **95**, 19311–19325.

Stixrude L. and Karki B. B. (2005) Structure and freezing of $MgSiO_3$ liquid in the Earth's lower mantle. *Science* **310**, 297–299.

Stixrude L. and Lithgow-Bertelloni C. (2005) Thermodynamics of mantle minerals. I. Physical properties. *Geophys. J. Int.* **162**, 610–632.

Stolper E. M., Walker D., Hager B. H. and Hays J. F. (1981) Melt segregation from partially molten source regions—the importance of melt density and source region size. *J. Geophys. Res.* **86**, 6261–6271.

Sugino O. and Car R. (1995) Ab-initio molecular-dynamics study of first-order phase-transitions—melting of silicon. *Phys. Rev. Lett.* **74**, 1823–1826.

Tangeman J. A., Phillips B. L., Navrotsky A., Weber J. K. R., Hixson A. D. and Key T. S. (2001) Vitreous forsterite (Mg$_2$SiO$_4$): synthesis, structure, and thermochemistry. *Geophys. Res. Lett.* **28**, 2517–2520.

Trønnes R. G. and Frost D. J. (2002) Peridotite melting and mineral-melt partitioning of major and minor elements at 22–24.5 GPa. *Earth Planet. Sci. Lett.* **197**, 117–131.

Vocadlo L., Alfe D., Gillan M. J. and Price G. D. (2003) The properties of iron under core conditions from first principles calculations. *Phys. Earth Planet. Interiors* **140**, 101–125.

Watt J. P. and Ahrens T. J. (1983) Shock compression of single-crystal forsterite. *J. Geophys. Res.* **88**, 9500–9512.

Williams Q. (1990) Molten (Mg$_{0.88}$Fe$_{0.12}$)$_2$SiO$_4$ at lower mantle conditions—melting products and structure of quenched glasses. *Geophys. Res. Lett.* **17**, 635–638.

Williams Q. and Garnero E. J. (1996) Seismic evidence for partial melt at the base of Earth's mantle. *Science* **273**, 1528–1530.

Williams Q., McMillan P. and Cooney T. F. (1989) Vibrational spectra of olivine composition glasses: the Mg–Mn join. *Phys. Chem. Miner.* **16**, 352–359.

Wolf G. H. and Jeanloz R. (1984) Lindemann melting law—anharmonic correction and test of its validity for minerals. *J. Geophys. Res.* **89**, 7821–7835.

Wolf G. H., Durben D. J. and McMillan P. F. (1990) High-pressure Raman spectroscopic study of sodium tetrasilicate (Na$_2$Si$_4$O$_9$) glass. *J. Chem. Phys.* **93**, 2280–2288.

Xue X., Stebbins J. F., Kanzaki M., McMillan P. F. and Poe B. (1991) Pressure-induced silicon coordination and tetrahedral structural changes in alkali oxide–silica melts up to 12 GPa: NMR, Raman, and infrared spectroscopy. *Am. Mineral.* **76**, 8–26.

Yeh I.-C. and Hummer G. (2004) System-size dependence of diffusion coefficients and viscosities from molecular dynamics simulations with periodic boundary conditions. *J. Phys. Chem. B* **108**, 15873–15879.

Zhang Y., Guo G., Refson K. and Zhao Y. (2004) Finite-size effect at both high and low temperatures in molecular dynamics calculations of the self-diffusion coefficient and viscosity of liquid silica. *J. Phys. Condens. Matter* **16**, 9127–9135.

Associate editor: Peter Ulmer